Plasmonic MIM and MSM Waveguide Couplers for Plasmonic Integrated Computing System

Samantha Lubaba Noor , *Graduate Student Member, IEEE*, Pol Van Dorpe , Dennis Lin,
Francky Catthoor , *Fellow, IEEE*, and Azad Naeemi , *Senior Member, IEEE*

Abstract—**Plasmonic metal-insulator-metal waveguide (MIM WG) is a promising building block of devices of a plasmonic computing system, and metal-semiconductor-metal (MSM) WG offers high-speed detection of plasmon signals. MIM and MSM WG couplers are an essential component of any integrated computing system that requires an interface between the plasmonic devices and the electronic circuits. However, the MIM and MSM WG couplers have not yet been explored and systematically studied. This work analyzes and benchmarks various coupling schemes of the plasmonic MIM and MSM WGs to single out the best coupling approach. From the detailed numerical analysis and considering the trade-offs among coupling loss, total capacitance, system noise, and bandwidth, a holistic metric is introduced to quantify and compare the system-level performance of the couplers, and a novel coupling scheme is identified as the most attractive choice for coupling the two WGs.**

Index Terms—**Energy per bit, MIM waveguide, plasmon detector, power transmission, waveguide coupling.**

I. INTRODUCTION

BEYOND CMOS (complementary metal oxide semiconductor) computing paradigms [1], [2] have gained considerable interest over the last few decades since CMOS circuits approach their scaling limits. Nevertheless, it is far from trivial to beat advanced scaled CMOS logic even when taking a metric like energy per binary switching [3], [4]. Photonic devices and components can be a possible substitute, with low propagation loss and ultra-high-speed attributes. However, the diffraction limit of light poses a strong challenge to the realization of nanoscale photonic devices. Surface Plasmon Polariton (SPP), an electromagnetic oscillation propagating along metal-dielectric interface, can overcome this scaling issue due to its subwavelength confinement while maintaining a potentially ultra-high throughput. Basically, both plasmonics and photonics have a similar bottleneck in terms of throughput and energy consumption: their throughput is limited by the coupler to the electronic domain, and energy consumption is dominated by the periphery (e.g.,

lasers and electronic excitation of the modulator, excitation for the final readout, etc.). However, SPPs can significantly increase the level of integration and miniaturization of the components, and hence offers an attractive overall area-throughput-energy (A-T-E) combination compared to their photonic counterparts.

Inspired by the unique opportunities of plasmonics for information processing, extensive theoretical and experimental investigations on plasmonic waveguides (WGs) and devices have been carried out recently. Some of the promising SPP-guiding geometries include nanoparticle chains [5], metal nanowires [6], metal-insulator-metal (MIM) WGs [7], [8], metal wedges [9], metallic grooves [10], and hybrid plasmonic WGs [11]. Among all the guiding geometries, the MIM WG is a potential platform for highly integrated plasmonic computing system since it supports propagating mode with nanoscale modal size [12] and provides deep-subwavelength field localization with substantial propagation length [13], [14]. As a result, MIM WGs have been employed repeatedly to design devices of a plasmonic computing system like logic gates [15], [16], phase and amplitude modulators [17], [18], power splitters [19], [20], frequency filters [21], [22], interconnect circuits [23], [24], and multiplexers [25].

For practical applications (e.g., readout purpose), the plasmonic MIM devices need to be interfaced with the CMOS circuit, which requires conversion of the plasmon signal to current/voltage. For an efficient conversion of the manipulated plasmon signal from a MIM device, a plasmonic MSM WG/detector [26] can be employed, which makes the coupler between the MIM and MSM WGs a crucial component for a highly integrated plasmonic computing system. Prior to an experimental study of the MIM and MSM WG couplers, a systematic theoretical study focusing on the quantitative comparison of the couplers is crucial as the cost of any experiment is getting extremely high with advanced scaled technology nodes making a wide space design exploration unaffordable. No previous study considered the coupling between the MIM and MSM WGs, to the best of our knowledge. This work aims to fill this gap. The main objective of our work is to explore the couplers for a highly integrated plasmonic computing system, for which the WG platform should be highly compact (WG width should be restricted to a few tens of nm); hence, we consider the coupling of MIM WG/WG-based devices and MSM WGs. Note that, in this work, we are not modeling the entire plasmonic computing system that also includes the hybrid photonic-plasmonic WG system [27], [28], plasmon excitation, plasmon modulators, CMOS circuits,
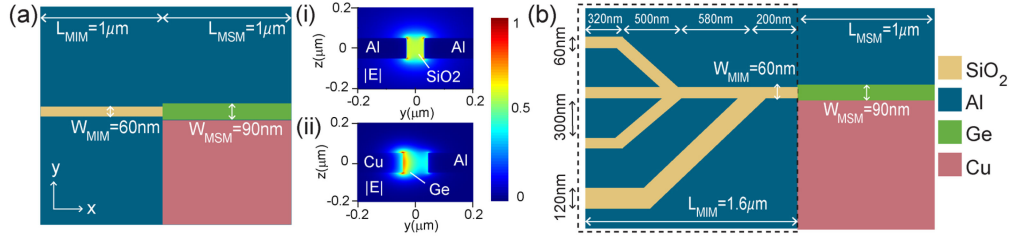
Fig. 1. 2D representation (top view) of the plasmonic MIM and MSM coupled structures considered in our simulations: (a) Case-A and (b) Case-B with the mode profiles shown for (i) MIM WG and (ii) MSM WG. For (b), the logic gate is shown in a box to represent that it can be considered a 'black box' containing any plasmonic MIM WG-based device.

which are beyond the scope of this paper. Additionally, MIM and MSM WGs have several other interesting applications [29]–[31], like biosensing, which is out of the scope of this paper since biosensing application has a much more relaxed requirement of input power and bandwidth (in the range of kHz [32]) compared to computing application.

The simplest way to couple a MIM and MSM WG is the end-butt coupling in which the metal claddings of both WGs are connected. However, the electrically connected metal cladding of the MIM WG increases the capacitive load of the detector by up to 25%, as shown in Section III B, thereby reducing the detection bandwidth. To address this challenge, we can electrically isolate the waveguide and detector using an insulating layer between the metal claddings of the two WGs. However, this insulating layer acts as an additional leakage path that weakens the coupling, and a holistic study is needed to evaluate whether or not it is beneficial to electrically insulate the two components. The two plasmonic WGs can also be directionally coupled. Earlier works explored the directional coupler of two similar plasmonic WGs [33], [34]. Is it efficient for the MIM-MSM WG coupling? Additionally, it was previously shown that plasmon can transmit through sharp bends over a wide frequency range [35]. Can we utilize this feature in coupling the two different WGs to have a compact and efficient coupler? In this work, using rigorous numerical simulations, we are going to address all these unexplored questions. From the detailed analysis of coupling loss, power transmission and absorption in the MSM WG, static and dynamic behavior and noise performance of the coupled WGs, and trade-offs among various performance parameters, we introduce a holistic metric to benchmark the couplers. Using the observations of our study, we have ultimately singled out a coupling scheme that excels in overall performance among all the choices.

II. PLASMONIC MIM AND MSM WG COUPLERS

To investigate the coupling between the plasmonic MIM and MSM WGs, we have designed an Al-SiO_2-Al MIM WG coupled to an Al-Ge-Cu MSM WG (Fig. 1(a)), which serves as a generic example of the coupled plasmonic WGs used for communicating data from the plasmonic into the electrical domain. To illustrate the use of the studied couplers in computing-related contexts, we additionally consider a single-stage Al-SiO_2-Al plasmonic logic gate (using the concept proposed by Dutta et al. [36]) coupled to Al-Ge-Cu

plasmonic detector [26] (Fig. 1(b)). The structures are embedded in SiO_2. The length and width of the WGs are labeled in Fig. 1, while the thickness of the WGs (h) and bottom oxide (t_{Box}) is $100nm$ and $1500nm$, respectively. The w_{MIM} and w_{MSM} values for the logic gate coupled detector are chosen to optimize the power transmission in the detector that ensures the characteristics impedance [37] matching of the WG sections. L_{MIM} of the generic MIM WG of Case-A is assumed $1\mu m$. For Case-B, L_{MIM} depends on the design of the majority gate (bending angle, input WG pitch etc.) and is taken from [36]. However, the conclusion of this work is independent of L_{MIM} as it only affects the loss in the MIM WG section.

We have performed a 3D fully-vectorial simulation of the coupled MIM-MSM structures using a commercially available 'Device Multiphysics Simulation Suite' of Lumerical Solution [38]. The optical simulations are performed using the state-of-the-art 3D finite difference time domain (FDTD) method. The fundamental mode is excited at the input MIM WG using Lumerical's mode source, which calculates the modes supported by a WG. The simulations are performed at optical communication wavelength, $\lambda = 1.31\mu m$, which ensures high power absorption in the Ge slot of the MSM detector. More details of the simulation parameters are given in section IV. The supported gap SPP modes, as shown in Fig. 1, have effective indices, $n_{eff(MIM,60nm)} = 1.75 + 0.03i$ and $n_{eff(MSM,90nm)} = 5.1 + 0.39i$.

Now we discuss the six coupling methods for plasmonic MIM and MSM WGs, which are illustrated in Fig. 2. The coupling methods are end-butt coupling, aligned coupling, overlap1, 2 coupling, directional coupling, and perpendicular/90° coupling. In the end-butt coupling, the WGs are coupled in a flush surface by directly placing a plasmonic MSM WG flat at the exit end of a MIM WG. In this coupling mechanism, the plasmonic MIM and MSM WGs are not electrically isolated since the metal claddings of the two WGs contact each other. In contrast, in the aligned coupler, a $5nm$ gap (filled with Al_2O_3) separates the metal claddings of the two WGs. In the overlap1 coupler, the metallic cladding (Al) on each side of the MIM slot continues towards the MSM WG in a step-like profile where it thins down to $5nm$ at the bottom of the MSM metal cladding. A $5nm$ ALD Al_2O_3 layer is used to separate the step-patterned metal layer from the MSM metal cladding, as illustrated in Fig. 2. In this coupling method, the Ge slot touches the bottom Al layer on both sides, which lowers the Schottky barrier height (SBH) at the metal-semiconductor junction due to Fermi level pinning [39]. In the overlap2 coupler, a $5nm$ thin continuous Al_2O_3 layer is
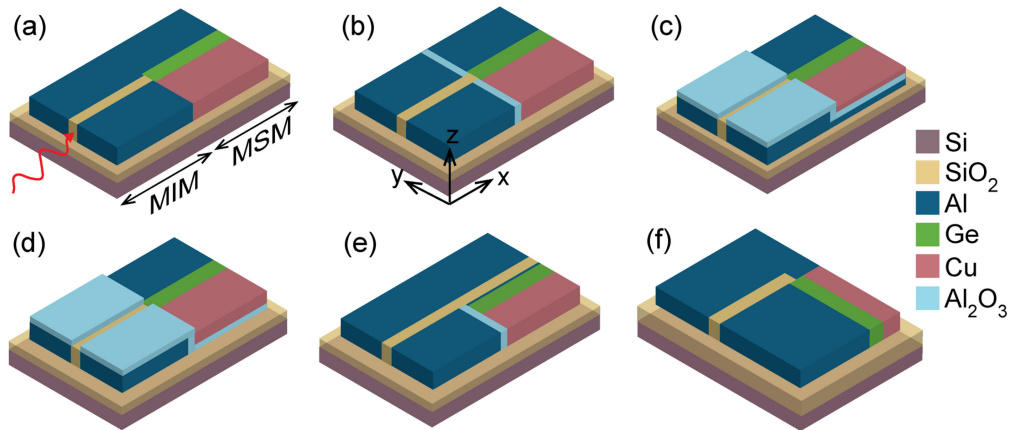
Fig. 2. Coupling methods between MIM and MSM plasmonic WGs: (a) end-butt coupling, (b) aligned coupling, (c) overlap1 coupling, (d) overlap2 coupling, (e) directional coupling, and (f) perpendicular coupling. WG cover layer is not shown.
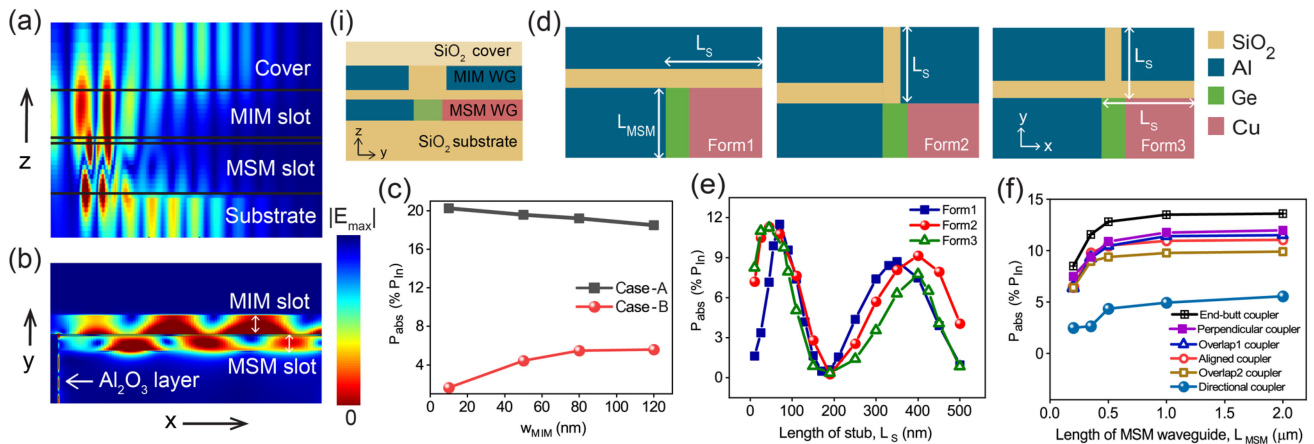

Fig. 3. Electric field in the directionally coupled WGs for (a) vertical coupling and (b) horizontal coupling. 2D cross-section of the vertical directionally coupled WGs is shown in (i) for clarity. (c) Effect of w_{MIM} on P_{abs} for the horizontal directional coupler. (d) Three forms of stub structures for the perpendicular coupler. (e) P_{abs} variation vs. stub length in the perpendicularly coupled WGs for the three forms of stubs shown in (d), and (f) P_{abs} vs. the length of MSM WG for all the six coupler designs. While (e) and (f) show the results for Case-B, similar trends are observed for Case-A.

deposited from the top of the MIM metal cladding to the bottom of the MSM metal cladding.

The two plasmonic WGs can also be coupled using a directional coupler by placing the Ge slot of the MSM WG close to the SiO_2 slot of the MIM WG. Unlike the conventional directional coupler in dielectric WGs, complete transfer of power from one WG to the other is not possible in this case due to the presence of the inherent loss in plasmonic WGs. The directional coupler can be horizontal or vertical. In the case of the vertical coupler, modes leak into one of the modes of the dielectric-metal-dielectric-metal-dielectric (DMDMD) structure formed by the two parallel metal films, which eliminates guiding of the modes [40]. For example, Fig. 3(a) and 3(b) show the field in the directionally coupled WGs for vertical (Fig. 3(a)(i)) and horizontal (Fig. 2(e)) coupling schemes, respectively. Cross-sectional areas of the MIM and MSM slots are $120nm \times 100nm$ and $90nm \times 100nm$, respectively. WG slots are separated by a $10nm$ thick (wide) SiO_2 (Al) layer for the vertical (horizontal) coupler. Field profile shows that mode is not guided in the WG slots for the vertical directional coupler. As a result, we consider the horizontal directional coupler in this study. In this coupler, a $5nm$ thin Al_2O_3 layer electrically isolates the metal claddings of the MSM WG, which act as electrodes of the MSM detector.

We also investigate a perpendicular coupler between the two WGs that includes a 90° bend. This scheme takes advantage of the high transmission possibility of a plasmon signal through sharp bends [35] to reduce the overall footprint of the coupled structure. For example, for the coupled devices of Case-B, the total area reduces by 20% if the perpendicular coupling is used instead of other coupling methods. Therefore, this scheme presents a clear advantage, given the crucial footprint metric in the A-T-E trade-off, as discussed in the introduction section. In summary, the end-butt and directional coupling are included in our study as they are commonly used coupling mechanisms in the photonic system. The aligned and overlap couplers are introduced to reduce the capacitive load contribution from the MIM WG by electrically isolating the two WGs. Lastly, the perpendicular coupler is introduced to have a reduced footprint of the coupled structures with reasonable coupling efficiency.

TABLE I
COMPARISON OF POWER LOSSES, ABSORPTION, AND REFLECTION FOR
DIFFERENT COUPLERS

Coupling Scheme	CL dB	IL dB		P_{abs} %P_{In}		R %P_{In}
		Case-A	Case-B	Case-A	Case-B	
End-Butt Coupler	0.38	1.75	3.7	23.3	13.5	4.6
Aligned Coupler	1.03	2.4	4	19	11	5.6
Overlap1 Coupler	0.76	2.1	4.4	21.8	11.4	9.8
Overlap2 Coupler	0.86	2.25	4.8	21	9.8	10.4
Directional Coupler	3.5	6.2	9.9	12.5	5	6
Perpendicular Coupler	0.65	2.8	4.5	21.7	11.8	4.6

III. RESULTS AND DISCUSSION

A. Coupling Loss, Power Reflection, and Absorption in the MSM WG

In this section, we evaluate the performance of different coupled structures in terms of their main efficiency-related figures-of-merit, namely coupling efficiency, coupling loss (CL), insertion loss (IL), coupling reflection (R), and power absorption in the active Ge region of the MSM WG (P_{abs}). The main difference between the two losses is CL includes only the loss due to coupling, whereas IL includes the propagation loss in the MIM WG and CL. CL and IL are obtained using the following relations [41]:

$$CL = -10log_{10}\eta \qquad (1)$$

$$IL = -10log_{10}T_{MSM} \qquad (2)$$

Here, η is the coupling efficiency, and T_{MSM} is the power transmitted in the MSM WG. Power transmission is measured using a 2D frequency-domain power monitor with the monitor area adjusted using a convergence testing to capture all the associated power. Moreover, power absorption inside the Ge slot is calculated as,

$$P_{abs} = -0.5\omega|E|^2 imag(\epsilon_{Ge}(\omega)) \qquad (3)$$

Here, E is the electric field inside the Ge slot and $imag(\epsilon_{Ge}(\omega))$ is the imaginary part of the dielectric constant. T_{MSM} and P_{abs} are calculated corresponding to the power injected at the input of the MIM WG section (P_{In}). For the logic gate case, measurements are taken when all the input bits are 1. We have also measured the reflection at the MIM WG-detector interface by injecting power just before the interface and placing a frequency-domain power monitor in front of the source that captures power transmission. Reflection is measured by deducting this transmission value from 1. Table I compares the figures-of-merit of different couplers for the two use cases.

Table I shows that most of the couplers exhibit $< 1dB$ coupling loss. Couplers with sub $1dB$ coupling loss are considered highly efficient couplers in dielectric WGs or Si photonics [42], [43], which indicates the sufficient efficiency of the coupling mechanisms considered in this study. The insertion loss that includes the propagation loss in the MIM WG section and WG-WG coupling loss is higher for Case-B because of the higher losses in the bends and junctions of the MIM logic gate compared to the lower propagation loss of the straight WG of

Case-A. The calculated SPP propagation loss of the MIM WG of Case-A is $\sim 1.24dB/\mu m$ and propagation length is $3.55\mu m$. Additionally, the group velocity of the SPP wave in the MIM WG is $1.6 \times 10^8 m/s$. Table I also shows that the power absorption in the Ge slot is maximum for the end-butt coupler. For the aligned coupler, we initially changed the width of the gap between the metal claddings of the WGs at the interface. As the gap width reduces from $20nm$ to $5nm$, power transmission improves by 34%. We have not considered gap widths less than $5nm$ to ensure less complexity in the device fabrication process. Moreover, reflection is high for the overlap couplers compared to the other coupling schemes.

From the loss and P_{abs} data of Table I, it is noticeable that the directional coupler is the weakest of all the coupling mechanisms due to large difference in the mode effective indices of the WGs. Coupling can be improved by decreasing (increasing) the width of the MIM (MSM) WG that increases (decreases) the $n_{eff(MIM)}$ ($n_{eff(MSM)}$) value. However, increasing w_{MSM} negatively affects the detection bandwidth of the MSM WG [26]. Therefore, we have changed w_{MIM} to improve the coupling. For the directional coupler of Case-A, as shown in Fig. 3(c), P_{abs} can be improved by 10% when w_{MIM} is reduced from $120nm$ to $10nm$. Conversely, for Case-B, a similar reduction of w_{MIM} at the WG interface decreases the P_{abs} value by 71%. This decrease is because the output of the logic gate needs to be tapered down to $10nm$, which results in high loss offsetting the effect of coupling improvement. Therefore, a trade-off exists between the coupling loss and tapering loss (bandwidth) when selecting w_{MIM} (w_{MSM}) for the directional coupler. We have used the optimized value of $w_{MIM} = 120nm$, keeping w_{MSM} unchanged for the directional coupler of Case-B in Table I. For the directional coupler of Case-A, $w_{MIM} = 120nm$ is also used since the $10nm$ width configuration is highly lossy.

For the perpendicular coupler, we have included a MIM stub [44] and analyzed the power absorption characteristics in the MSM waveguide. For P_{abs} analysis, we have considered three different forms of stub: two single-stub and a double-stub structure. Fig. 3(d) shows the three forms of stub where stub length is denoted as L_s. We have studied the dependence of P_{abs} on L_s keeping the width the same as w_{MIM}. The dependence, as shown in Fig. 3(e), originates from the variation of power transmission due to the interference between the SPP signals passing through and returning from the stub [44]. Although the transmitted power varies periodically with L_s, peak transmission/absorption in the MSM WG falls when L_s increases since the SPP signal returning from the stub decays as the signal propagates a longer path. In Table I, for the perpendicular couplers, we have used the Form 1 stub with $L_s = 70nm$ for both the cases, which provide maximum power absorption in Ge.

For all the coupled configurations, we also analyze the effect of length variation of the MSM WG, as shown in Fig. 3(f). For $L_{MSM} > 1\mu m$, the absorption profiles almost saturate, indicating that most of the power has already been absorbed in Ge. For this reason, in our simulations, we have chosen $L_{MSM} = 1\mu m$ for all the couplers.
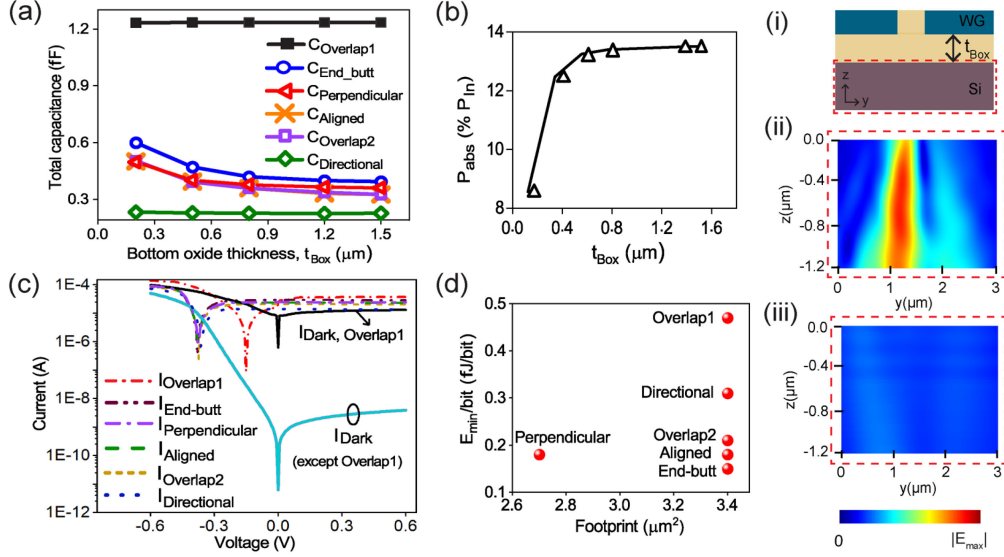
Fig. 4. (a) Total capacitance of the coupled structures with $C_{Overlap1}$ shown as $1/5^{th}$ of the original values (b) Power absorption in Ge for changing t_{Box} with field profile, $|E|$ in the Si substrate shown for (ii) $t_{Box} = 200nm$ and (iii) $1500nm$ at the output of the MIM WG ($x = 1.6\mu m$), (c) Static characteristics, and (d) comparison of performance metrics of all the coupled plasmonic structures. All plots are for Case-B, and Case-A shows similar trends.

B. Total Capacitance of the Coupled Structures

Next, we analyze the total capacitance of the coupled plasmonic structures. We have used the 3D field solver of Raphael, Synopsys [45] to find the equivalent capacitance of the structures. The detail is explained in section IV. Since the WGs are metallic structures, total resistance and its variation among different couplers are small. Consequently, the total capacitance affects delay and bandwidth, and hence the overall performance of the coupled WGs. Simulation results show that at $t_{Box} = 1500nm$, the detector's intrinsic capacitance is $0.311fF$, and end-butt coupled MIM WG section increases the capacitive load of the detector by 25.4%. As t_{Box} becomes smaller, a noticeable capacitive load is added by the end-butt coupled MIM WG section (for example, capacitive load increases by 64.2% at $t_{Box} = 200nm$). Electrical isolation of the two WGs using a thin dielectric layer helps to reduce the capacitive load, as shown in Fig. 4(a) for the aligned and overlap2 coupler. Additionally, the total capacitance of the overlap1 coupled structure is an order of magnitude higher than that of the other coupled structures, which can be attributed to the presence of thin Al_2O_3 film in between the MSM WG's electrodes and the bottom Al film. Consequently, t_{Box} has a negligible influence on the capacitance of this coupler. Moreover, for the directional coupler, equivalent capacitance is small due to the narrow metal cladding of the MSM WG.

The thickness of the bottom oxide layer also affects the power absorption in the MSM WG, as shown in Fig. 4(b). As t_{Box} drops below $600nm$, power absorption in Ge decreases, which can be explained from the field profile of Fig. 4(b)(ii)-(iii). When the bottom oxide is made thinner, the field penetrates the Si substrate (Fig. 4(b)(ii)) resulting in less power transfer to the MSM WG. For example, for the end-butt coupler of Case-B, $t_{Box} = 200nm$ results in a 26% reduction in the power transmission (T_{MSM})

compared to when a $1500nm$ thick bottom oxide layer is used. For this reason, we have considered $t_{Box} = 1500nm$ for all simulations.

C. A Holistic Performance Metric: Minimum Detectable Energy per Bit

Now we analyze the performance of the coupled MSM WG as a plasmonic detector. The electric field (E) and permittivity data ($\epsilon_{Ge}(\omega)$) obtained from the FDTD simulation are used to find the photogeneration rate (G) in Ge, which is imported in the 'Device Charge Transport' solver of Lumerical to simulate the static and dynamic responses of the MSM WG. G is calculated using the following relation:

$$G = \frac{-0.5|E|^2 Im(\epsilon_{Ge}(\omega))}{\hbar} \qquad (4)$$

To incorporate non-ideality of carrier mobility and lifetime, several models are included in the simulation, which are explained in Section IV.

Fig. 4(c) studies the steady-state behavior of the MSM WG. The current in the presence of SPP signal deviates for various coupling methods depending on the amount of power being absorbed in the Ge slot. For the overlap1 coupler, dark current (I_{Dark}) is high because of the presence of Al on both sides of the Ge slot that reduces the SBH at the metal-semiconductor junction [26], [39]. The high I_{Dark} makes detection of the weakest output signal of the overlap1 coupled logic gate very challenging. We have also investigated the dynamic performance of the MSM detectors by performing transient simulations. The calculated transit time-limited bandwidth of the detectors is $260GHz$. Additionally, the RC-limited bandwidth is calculated considering the total capacitance of the coupled structures and

Coupling Scheme	Case-A fJ/bit	Case-B fJ/bit
End-Butt Coupler	0.08	0.15
Aligned Coupler	0.1	0.18
Overlap1 Coupler	0.25	0.47
Overlap2 Coupler	0.1	0.21
Directional Coupler	0.15	0.31
Perpendicular Coupler	0.09	0.18

a load of $R_{Load} = 1K\Omega$, $C_{Load} = 1fF$ for the detector. Although the system bandwidth is RC-limited for the considered load condition, the overlap1 coupled structure has much lower bandwidth compared to all the other options because of the large capacitance of the MSM WG. For instance, for Case-B, bandwidth of the end-butt coupled structure is 110 GHz, whereas bandwidth is 22 GHz (5X lower) for the Overlap1 coupled structure. The intrinsic resistance of the detector is not considered during the bandwidth calculation since the metallic lateral claddings of the detector can be used as low resistive contacts [46].

Next, we consider the noise of the detector, which can be quantified by the noise equivalent power (NEP). NEP, the incident light power on the detector below which the photocurrent can no longer be distinguished from the noise current, is represented by [26],

$$NEP = \frac{i_n P_{in,d}}{I_P} \qquad (5)$$

Here, i_n, $P_{in,d}$, I_p represent noise current, detector's input power, and photocurrent, respectively. i_n includes the shot noise of the detector and thermal noise of the detector and the load resistance. Using the calculated NEP of each detector and noise bandwidth ($\frac{\pi}{2}$ bandwidth), we estimate the corresponding power (P_{min}) required at the input of the MIM section. Next, we determine the minimum energy threshold required to detect a single bit sent from the MIM side (E_{min}/bit) by taking the ratio of P_{min} and the system bandwidth.

The E_{min}/bit value encompasses the coupling and insertion loss, power transmission and absorption in the MSM WG, noise in the detector, and the detection bandwidth: all the critical performance parameters of the coupled WGs that we have discussed so far. A coupled structure can have high power absorption in the MSM WG but low detection bandwidth (e.g., overlap1 coupled WGs), or it can offer high bandwidth with low power absorption (e.g., directionally coupled WGs) capability. A metric is required that reflects the effect of all the figures-of-merit of the coupled structures. The most important goal in computing is to compute as much data as possible with as little energy as possible. One can consider minimizing the required energy per bit threshold as the ultimate goal for low power computing. By tying the performance of the couplers to energy/bit, we can come up with the best coupling approach that gives the best balance between the power and bandwidth; hence, E_{min}/bit is a holistic metric to compare the couplers.

Table II compares the required E_{min}/bit values for all the couplers. From the table we can observe that the lowest and the highest E_{min}/bit values correspond to the end-butt coupler and the overlap1 coupler, respectively. The high value of the overlap1 coupled structure can be attributed to the high shot noise current (due to high I_{Dark}) and low bandwidth. Table II also shows that E_{min}/bit of the horizontal directional coupler is noticeably higher than the other couplers (except overlap1) due to the weak coupling of the WGs. For the aligned, overlap2, and perpendicular couplers, E_{min}/bit are roughly equal. The perpendicular coupler offers an added benefit of less area requirement, as discussed earlier, while its E_{min}/bit requirement is very close to the end-butt minimum. Although end-butt coupling is the most energy-efficient scheme, it is not the optimum one. Footprint is also a crucial metric to evaluate the coupled system, given that miniaturization is the key advantage of plasmonic devices over their photonic counterparts. Considering the trade-off between energy per bit and footprint (Fig. 4(d)), the perpendicular coupler can be considered the best choice for coupling plasmonic MIM and MSM WGs.

Note that, although plasmonic MIM WGs are lossy ($< 10\mu m$ propagation length), we focus on very compact devices like the ultra-high throughput majority gate [36]. Such a gate can implement many functions by simply adjusting the threshold voltage of the CMOS receiver [47], which would be impossible to achieve with CMOS and would require many transistors while still operating at much lower frequencies. We emphasize that although in this work, we consider plasmonic MIM logic gate for demonstrating the system-level performance of the couplers, the couplers are applicable for coupling any MIM WG-based devices [15]–[25] with the MSM WG. Hence the findings of this work will provide design guidelines and theoretical insight for all the researchers who work on plasmonic devices for an integrated computing system.

1) Effect of Receiver Circuit on the Holistic Metric: The output signal of the coupled plasmonic detector is processed in the receiver circuit, which acts as the load of the detector. We consider a theoretical parallel RC circuit model for the receiver and now we are going to quantify the impact of the receiver circuit parameters (R_{Load}, C_{Load}) on the holistic performance metric of the couplers. R_{Load} affects both the system noise (i_n) and bandwidth. Thermal noise contribution of R_{Load} primarily dominates the overall system noise since except the overlap1 coupler case, the plasmonic detector under consideration has a very low shot and thermal noise due to the low I_{Dark} and high dark shunt resistance ($M\Omega$ range), respectively. Increasing R_{Load}, therefore, helps to reduce the E_{min}/bit by reducing i_n as long as bandwidth is transit time-limited, as shown in Fig. 5(a). The further increase in R_{Load} causes a similar decrease of i_n and bandwidth, keeping E_{min}/bit constant. However, if R_{Load} is very high ($> 1M\Omega$ for Fig. 5(a)), i_n does not significantly change, and bandwidth reduction increases E_{min}/bit as R_{Load} increases. For the overlap1 coupler, the detector's intrinsic noise mostly governs the total noise, and the change of bandwidth controls E_{min}/bit as R_{Load} varies. As a result, with the increase of R_{Load}, E_{min}/bit continuously increases when the bandwidth is RC-limited. Apart from R_{Load}, C_{Load} also affects E_{min}/bit: an increase in C_{Load} increases E_{min}/bit due to the reduction of bandwidth, as shown in Fig. 5(b).
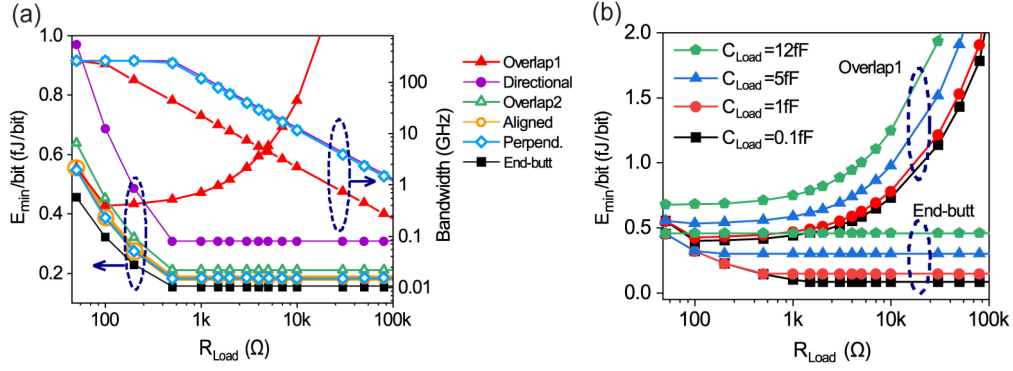
Fig. 5. Effect of receiver circuit parameters on E_{min}/bit of the couplers. For (a), $C_{Load} = 1fF$ and effect of R_{Load} on the system bandwidth is shown on the right y-axis. For (b), plots for the other four couplers are not shown since they follow a similar performance trend as the end-butt coupler.
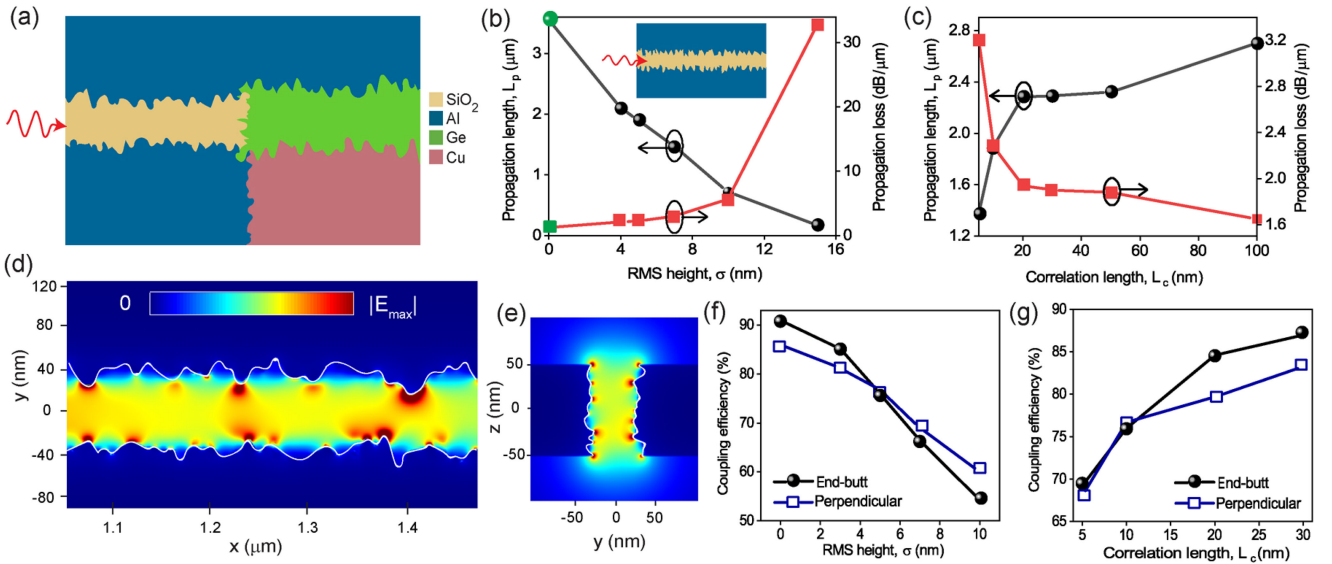

Fig. 6. (a) 2D view of the coupled plasmonic MIM and MSM WGs with rough interfaces. Effect of (b) σ and (c) L_c on the propagation properties of SPP mode in the MIM WG. Electric field profile in the rough MIM WG in the (d) xy and (e) yz direction. Effect of (f) σ and (g) L_c on the coupling efficiency of the coupled WGs. $L_c = 10nm$ for (b) and (f), $\sigma = 5nm$ for (c) and (g). $\sigma = 0$ represents the smooth WG.

2) Effect of Roughness in the Plasmonic WGs: The plasmonic WGs may suffer from random surface irregularity/roughness due to fabrication imperfection. As the SPP signal propagates along the metal-dielectric interface, roughness at the interface can alter the mode profile and propagation properties. In this section, we analyze the effect of the rough metal-dielectric interface on the performance of the WGs and coupling mechanisms. The roughness of a randomly patterned surface can be numerically modeled using a root-mean-square (RMS) height (σ) and a correlation length (L_c) [48], [49]. We assume that the roughness function, $h(r)$ obeys normal/Gaussian distribution with zero mean and σ, L_c are related to the autocorrelation function by [49],

$$< h(r)h(r + \delta) >= \sigma^2 exp\left(-\delta^2/L_c^2\right) \quad (6)$$

We consider mutually uncorrelated surface roughness at all metal-dielectric, metal-metal, dielectric-semiconductor, and metal-semiconductor interfaces and sidewalls of the MIM and MSM WGs (Fig. 6(a)).

To model the surface roughness in the solver, we first create a matrix of random numbers in k space and then apply the correlation length and Gaussian shape (Gaussian function in real space is mapped to another Gaussian function with a different width in k space). The resulting values are transformed back to real space, and RMS height is adjusted to generate the random patterns. The effect of random nature of roughness can be suppressed by averaging the results obtained from several different random samples [50]. Therefore, for each σ and L_c values, simulation results are obtained by averaging the results of five different samples of randomly generated rough WGs.

We first study the mode properties of the rough MIM WG by calculating the mode propagation loss and propagation length (L_p) for different σ and L_c using the Transmission coefficient (T) through the WG of length L. $ln(T)$ undergoes a linear variation with L [49], from which we calculate L_p of the rough MIM

WGs:

$$ln(T) = -L/L_p \tag{7}$$

Fig. 6(b) shows that with the increase of σ, SPP propagation loss increases which decreases L_p. Here, $\sigma = 0nm$ represents the smooth MIM WG. Surface roughness causes additional damping of SPP signal on top of the intrinsic loss due to scattering and reflection of the waves at rough metal-dielectric interfaces. For large σ ($\sigma > 10nm$), excess signal attenuation due to roughness severely affects the mode resulting in a L_p of few nm. The impact of variation in L_c on SPP mode of the MIM WG is shown in Fig. 6(c). An increase in L_c makes the interfaces smoother, resulting in lower scattering, lower loss, and a longer mode propagation length. For very large L_c ($Lc > 100nm$), the WG surfaces are almost flat and consequently, L_p is very close to the smooth WG case. We also study the electric field profile of the rough MIM WG. The field intensity in the dielectric slot is enhanced at the peak of the metal roughness bumps, as shown in Fig. 6(d)-(e). The field enhancement results from the crowding of the electric field lines in the dielectric due to increased surface charge density at the metal bump peaks, which is commonly known as the 'lightning rod effect' [51].

We next study the coupling performance of the MIM and MSM WGs considering roughness at the WGs and WG interfaces. Because of increased reflection, coupling efficiency reduces as σ increases, as shown in Fig. 6(f). Also, Fig. 6(g) shows that coupling efficiency improves and reaches close to the smooth WG value as L_c increases due to the reduced roughness effect. Due to higher propagation loss and reduced coupling efficiency, roughness increases the E_{min}/bit value of the coupled WGs. For example, for the end-butt coupled WGs of Case-A, as σ increases from $0nm$ to $5nm$, E_{min}/bit increases from $0.08fJ/bit$ to $0.29fJ/bit$ when $L_c = 10nm$.

In short, roughness introduces additional SPP propagation loss in the WGs and reduces the coupling efficiency, which eventually increases the E_{min}/bit value of the coupled WGs. The WG sidewall roughness is defined primarily by the line edge roughness (LER) of resist used for patterning. Experimentally it was shown that the LER of the electron beam lithography process ranges between $\sigma = 0.47 - 0.75nm$ with $L_c = 25.9 - 66.9nm$ [52] for a photonic WG. Using Fig. 6(f) we can say that with the surface smoothness achievable in the state-of-the-art semiconductor manufacturing setting, one can expect less than 3% increase in loss compared to the ideal case. Hence, using a proper patterning technology, the roughness and consequently associated losses can be reduced for the coupled plasmonic WGs.

IV. SIMULATION METHOD

The FDTD method used for optical simulations solves the time-dependent Maxwell's equation on a discrete grid in both space and time. Perfectly matched layer (PML) absorbing boundary conditions are used at all the boundaries of the simulation region. Conformal meshing [53] is used in the simulation with a mesh size of $5nm$. The dispersive dielectric constants of the materials, obtained from Palik's 'Handbook of Optical Constants' [54] are, $\epsilon_{SiO_2} = 2.09$, $\epsilon_{Al} = -174 + 32.67i$, $\epsilon_{Cu} = -48.95 + 7.18i$, and $\epsilon_{Ge} = 18.5 + 0.67i$ at $\lambda = 1310nm$.

In the 'Device Charge Transport' solver, materials are defined using their workfunction values ($\phi_{Al} = 4.28eV$, $\phi_{Cu} = 4.65eV$, and $\phi_{Ge} = 4.5eV$). For Ge, bandgap ($E_g = 0.659eV$), intrinsic carrier concentration ($n_i = 1.84 \times 10^{13}cm^{-3}$), and carrier effective mass ($m_n = 0.56m_e$, $m_p = 0.29m_e$) are indicated. The simulations include Caughey Thomas model [55] and Canali model [56], which incorporate the impurity scattering effect and carrier velocity saturation effect, respectively. According to the models,

$$\mu = \frac{\mu_1}{\left(1 + \left(\frac{\mu_1 F}{v_{sat}}\right)^{\beta}\right)^{1/\beta}} \tag{8}$$

$$\mu_1 = \mu_{min} + \frac{\mu_L - \mu_{min}}{1 + (N/N_{ref})^{\alpha}} \tag{9}$$

Here, F is calculated from the quasi-Fermi level gradient, v_{sat} = carrier saturation velocity = $6 \times 10^6 cms^{-1}$, μ_1 = mobility after applying the Caughey Thomas model, and N = doping density = $5 \times 10^{16}cm^{-3}$. For electron, $\alpha = 0.56$, $\beta = 2$, $\mu_{min} = 850cm^2/Vs$, $\mu_L = 3900cm^2/Vs$, and $N_{ref} = 2.6 \times 10^{17}cm^{-3}$. For hole, $\alpha = \beta = 1$, $\mu_{min} = 300cm^2/Vs$, $\mu_L = 1800cm^2/Vs$, and $N_{ref} = 10^{17}cm^{-3}$. Moreover, the bulk Shockley-Read-Hall (SRH) recombination model is included in simulation with carrier lifetime, $\tau_0 = 50ps$. Lifetime correction for doping effect is also included by considering the Fossum model [57]:

$$\tau' = \frac{\tau_0}{1 + N/N_0} \tag{10}$$

Here, $N_0 = 7.1 \times 10^{15}cm^{-3}$. Additional lifetime correction for trap-assisted tunneling effect is incorporated in simulation by including the Hurkx model [58]. In the Hurkx model, the correction term depends on the parameter, $m_t = 0.55$ (for electron), 0.19 (for hole). The non-ideality of the Ge surface is also considered in the simulation by including the surface SRH model with a surface recombination velocity of $2.25 \times 10^5 cms^{-1}$ at the Ge-SiO_2 interface.

We have additionally used the Finite Difference Eigenmode (FDE) solver of Lumerical to calculate the mode effective indices for varying signal frequency/wavelength and consequently the SPP group velocity for the MIM WG. Lastly, to compute the capacitance of the coupled plasmonic WGs, we have employed the 3D field solver of Raphael, Synopsys [45], which is based on the finite difference method. It solves the Poisson equation and calculates the capacitance matrix for the electrodes, from which we have calculated the total capacitance of the coupled structures using equivalent capacitance equations. To demonstrate how we calculate the total capacitance, Fig. 7(a) shows the end-butt coupled plasmonic devices of Case-B with labeled electrodes, and Fig. 7(b) shows the equivalent circuit used for capacitance calculation.

To ensure that our simulations are producing accurate data, we have tested a reference MIM WG fabricated in [59] and calculated its propagation length (L_{p1}). Our calculated $L_{p1}(10.4\mu m)$
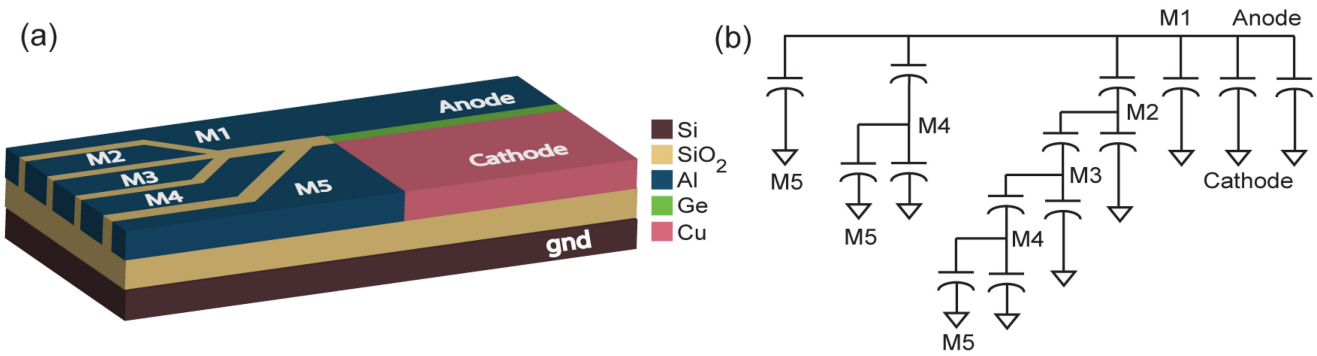
Fig. 7. (a) The coupled plasmonic devices (end-butt coupling) of Case-B with labeled electrodes and (b) corresponding equivalent circuit for capacitance calculation.

is close to the theoretical value mentioned in the paper ($10.9\mu m$). Experimental value of L_{p1} is $5.5\mu m$ [59], and the authors in the paper have attributed the discrepancy to the WG sidewall roughness. Using our roughness model, we have found that when RMS height, $\sigma = 6nm$ and correlation length, $L_c = 10nm$, L_{p1} reduces to $5.5\mu m$ and matches the measured data.

V. CONCLUSION

In conclusion, we present a thorough analysis and benchmark the possible schemes for coupling plasmonic MIM and MSM waveguides (WGs). In addition to the generic MIM and MSM WG, we demonstrate the application and system-level performance of the couplers for plasmonic MIM device by considering a MIM logic gate as an example. Our simulation results show that the performance trends of the couplers are similar for both the cases. It is found that among all the schemes, the end-butt coupler results in maximum power transmission and the highest photocurrent (I_p) in the MSM detector. However, the two WGs are electrically connected in this coupling approach. Introducing a thin dielectric layer between the metal cladding electrically isolates the two WGs at the cost of a decreased I_p due to the reduced power transmission. We also explore couplers where MSM WG's cladding overlaps the metal or dielectric cladding of the MIM WG and observe that the former one results in higher capacitance ($\sim 10\times$) and dark current ($\sim 10^4\times$) compared to all the other coupling options. Moreover, the directional coupling between the WGs is found to be weak because of the large difference in the mode effective indices. Additionally, a perpendicular coupler is proposed for which a MIM stub is incorporated and optimized to improve the power transmission. All the coupled WGs require the same footprint except the perpendicular one that ensures a more compact structure. Lastly, we introduce a holistic performance metric, minimum detectable energy per bit threshold (E_{min}/bit), which encompasses coupling loss, power transmission, total capacitance, detector's noise current, I_p, and detection bandwidth. The calculated E_{min}/bit value is the lowest for the end-butt coupled structure. However, our results show that apart from the coupler with overlapping metal configuration, all the coupling schemes produce comparable E_{min}/bit values. Since the perpendicular coupler additionally features the lowest footprint, it can be considered the best choice

for coupling plasmonic MIM and MSM WGs. We have also analyzed the effect of the receiver circuit on E_{min}/bit using a theoretical circuit model. We have additionally studied the effect of surface roughness on the performance of the plasmonic WGs and couplers. The analysis and results presented in this work will be critical for designing a plasmonic integrated computing system that incorporates co-integration of plasmonic devices and electronic circuits for high-end server system applications.

REFERENCES

[1] J. J. Yang, D. B. Strukov, and D. R. Stewart, "Memristive devices for computing," *Nature Nanotechnol.*, vol. 8, no. 1, pp. 13–24, 2013.

[2] S. Manipatruni, D. E. Nikonov, and I. A. Young, "Beyond CMOS computing with spin and polarization," *Nature Phys.*, vol. 14, no. 4, pp. 338–343, 2018.

[3] D. E. Nikonov and I. A. Young, "Benchmarking of beyond-CMOS exploratory devices for logic integrated circuits," *IEEE J. Explor. Solid-State Computat.*, vol. 1, pp. 3–11, Dec. 2015.

[4] R. M. Iraei *et al.*, "Clocked magnetostriction-assisted spintronic device design and simulation," *IEEE Trans. Electron Devices*, vol. 65, no. 5, pp. 2040–2046, May 2018.

[5] S. A. Maier *et al.*, "Local detection of electromagnetic energy transport below the diffraction limit in metal nanoparticle plasmon waveguides," *Nature Mater.*, vol. 2, no. 4, pp. 229–232, 2003.

[6] A. L. Pyayt, B. Wiley, Y. Xia, A. Chen, and L. Dalton, "Integration of photonic and silver nanowire plasmonic waveguides," *Nature Nanotechnol.*, vol. 3, no. 11, pp. 660–665, 2008.

[7] J. Chen, G. A. Smolyakov, S. R. Brueck, and K. J. Malloy, "Surface plasmon modes of finite, planar, metal-insulator-metal plasmonic waveguides," *Opt. Exp.*, vol. 16, no. 19, pp. 14902–14909, 2008.

[8] H. Lu, G. Wang, and X. Liu, "Manipulation of light in MIM plasmonic waveguide systems," *Chin. Sci. Bull.*, vol. 58, no. 30, pp. 3607–3616, 2013.

[9] A. Boltasseva, V. S. Volkov, R. B. Nielsen, E. Moreno, S. G. Rodrigo, and S. I. Bozhevolnyi, "Triangular metal wedges for subwavelength plasmon-polariton guiding at telecom wavelengths," *Opt. Exp.*, vol. 16, no. 8, pp. 5252–5260, 2008.

[10] D. Arbel and M. Orenstein, "Plasmonic modes in w-shaped metal-coated silicon grooves," *Opt. Exp.*, vol. 16, no. 5, pp. 3114–3119, 2008.

[11] X. Yang, Y. Liu, R. F. Oulton, X. Yin, and X. Zhang, "Optical forces in hybrid plasmonic waveguides," *Nano Lett.*, vol. 11, no. 2, pp. 321–328, 2011.

[12] E. N. Economou, "Surface plasmons in thin films," *Phys. Rev.*, vol. 182, no. 2, 1969, Art. no. 539.

[13] R. Zia, M. D. Selker, P. B. Catrysse, and M. L. Brongersma, "Geometries and materials for subwavelength surface plasmon modes," *J. Opt. Soc. Amer. A*, vol. 21, no. 12, pp. 2442–2446, 2004.

[14] J. Dionne, H. Lezec, and H. A. Atwater, "Highly confined photon transport in subwavelength metallic slot waveguides," *Nano Lett.*, vol. 6, no. 9, pp. 1928–1932, 2006.

[15] J. Chai *et al.*, "A novel manipulation for implementing logic operations based on plasmonic resonators," *IEEE Photon. J.*, vol. 11, no. 1, Feb. 2019, Art. no. 2700110.

[16] Y. Ye *et al.*, "A novel multi-functional plasmonic logic device by angle manipulation," *IEEE Trans. Nanotechnol.*, vol. 19, pp. 94–101, 2020.

[17] S. Kamada, T. Okamoto, S. E. El-Zohary, and M. Haraguchi, "Design optimization and fabrication of Mach-Zehnder interferometer based on MIM plasmonic waveguides," *Opt. Exp.*, vol. 24, no. 15, pp. 16224–16231, 2016.

[18] C. Haffner *et al.*, "Low-loss plasmon-assisted electro-optic modulator," *Nature*, vol. 556, no. 7702, pp. 483–486, 2018.

[19] M. A. Butt, S. N. Khonina, and N. L. Kazanskiy, "Ultra-short lossless plasmonic power splitter design based on metal–insulator–metal waveguide," *Laser Phys.*, vol. 30, no. 1, 2020, Art. no. 0 16201.

[20] Y. Ye *et al.*, "Design of a novel plasmonic splitter with variable transmissions and selectable channels," *IEEE Trans. Nanotechnol.*, vol. 18, pp. 617–625, 2019.

[21] Y. Qi *et al.*, "Theoretical study of a multichannel plasmonic waveguide notch filter with double-sided nanodisk and two slot cavities," *Results Phys.*, vol. 14, 2019, Art. no. 102506.

[22] S. Khani, M. Danaie, and P. Rezaei, "Tunable single-mode bandpass filter based on metal–insulator–metal plasmonic coupled u-shaped cavities," *IET Optoelectron.*, vol. 13, no. 4, pp. 161–171, 2019.

[23] A. Shaaban, Y.-C. Du, and L. R. Gomaa, "Transmissivity assessment of plasmonic-dielectric waveguide interconnects via modified FFT-BPM," *Optik*, vol. 208, 2020, Art. no. 164143.

[24] P. Yeonsang, R. Younggeun, K. Jineun, and L. Changwon, "Light interconnection device using plasmonic via," U.S. Patent 9,715,063, 2017.

[25] Y.-D. Wu, "High transmission efficiency wavelength division multiplexer based on metal–insulator–metal plasmonic waveguides," *J. Lightw. Technol.*, vol. 32, no. 24, pp. 4844–4848, 2014.

[26] S. L. Noor *et al.*, "Modeling and optimization of plasmonic detectors for beyond-CMOS plasmonic majority logic gates," *J. Lightw. Technol.*, vol. 38, no. 18, pp. 5092–5099, 2020.

[27] M. P. Nielsen *et al.*, "Adiabatic nanofocusing in hybrid gap plasmon waveguides on the silicon-on-insulator platform," *Nano Lett.*, vol. 16, no. 2, pp. 1410–1414, 2016.

[28] L. Lafone, T. P. Sidiropoulos, and R. F. Oulton, "Silicon-based metal-loaded plasmonic waveguides for low-loss nanofocusing," *Opt. Lett.*, vol. 39, no. 15, pp. 4356–4359, 2014.

[29] F. Dell'Olio, D. Conteduca, M. De Palo, and C. Ciminelli, "Design of a new ultracompact resonant plasmonic multi-analyte label-free biosensing platform," *Sensors*, vol. 17, no. 8, 2017, Art. no. 1810.

[30] S. Kumar and R. Singh, "Recent optical sensing technologies for the detection of various biomolecules," *Opt. Laser Technol.*, vol. 134, 2021, Art. no. 106620.

[31] V. E. Babicheva, R. Malureanu, and A. V. Lavrinenko, "Plasmonic finite-thickness metal–semiconductor–metal waveguide as ultra-compact modulator," *Photon. Nanostructures-Fundamentals Appl.*, vol. 11, no. 4, pp. 323–334, 2013.

[32] M. A. Awan, B. Wang, N. A. Quadir, and A. Bermak, "Review and analysis of CMOS current readout circuits for biosensing applications," in *Proc. IEEE Int. Symp. Circuits Syst.*, 2021, pp. 1–5.

[33] D. Gramotnev, K. Vernon, and D. Pile, "Directional coupler using gap plasmon waveguides," *Appl. Phys. B*, vol. 93, no. 1, pp. 99–106, 2008.

[34] H. Zhao, X. G. Guang, and J. Huang, "Novel optical directional coupler based on surface plasmon polaritons," *Physica E: Low-dimensional Syst. Nanostructures*, vol. 40, no. 10, pp. 3025–3029, 2008.

[35] G. Veronis and S. Fan, "Bends and splitters in metal-dielectric-metal subwavelength plasmonic waveguides," *Appl. Phys. Lett.*, vol. 87, no. 13, 2005, Art. no. 131102.

[36] S. Dutta *et al.*, "Proposal for nanoscale cascaded plasmonic majority gates for non-boolean computation," *Sci. Rep.*, vol. 7, no. 1, Art. no. 17866, 2017.

[37] W. Cai, W. Shin, S. Fan, and M. L. Brongersma, "Elements for plasmonic nanocircuits with three-dimensional slot waveguides," *Adv. Mater.*, vol. 22, no. 45, pp. 5120–5124, 2010.

[38] Lumerical Solutions, [Online]. Available: https://www.lumerical.com

[39] A. Dimoulas, P. Tsipas, A. Sotiropoulos, and E. K. Evangelou, "Fermi-level pinning and charge neutrality level in germanium," *Appl. Phys. Lett.*, vol. 89, no. 25, 2006, Art. no. 252110.

[40] G. Veronis and S. Fan, "Crosstalk between three-dimensional plasmonic slot waveguides," *Opt. Exp.*, vol. 16, no. 3, pp. 2129–2140, 2008.

[41] R. Sattibabu, B. S. Bhaktha, and P. Ganguly, "Estimation of fiber-waveguide coupling loss and waveguide propagation loss by spectral analysis," *IEEE Photon. Technol. Lett.*, vol. 31, no. 7, pp. 517–520, Apr. 2019.

[42] R. S. Tummidi and M. Webster, "Multilayer silicon nitride-based coupler integrated into a silicon photonics platform with< 1 db coupling loss to a standard SMF over O, S, C and L optical bands," in *Proc. Opt. Fiber Commun. Conf. Exhib.*, 2020, Paper Th2A.10.

[43] C. Hu *et al.*, "High-efficient coupler for thin-film lithium niobate waveguide devices," *Opt. Exp.*, vol. 29, no. 4, pp. 5397–5406, 2021.

[44] Y. Matsuzaki, T. Okamoto, M. Haraguchi, M. Fukui, and M. Nakagaki, "Characteristics of gap plasmon waveguide with stub structures," *Opt. Exp.*, vol. 16, no. 21, pp. 16314–16325, 2008.

[45] Raphael, Synopsys Inc., [Online]. Available: https://www.synopsys.com/silicon/tcad/interconnect-simulation/raphael.html

[46] Y. Salamin *et al.*, "100 GHz plasmonic photodetector," *ACS Photon.*, vol. 5, no. 8, pp. 3291–3297, 2018.

[47] E. Testa *et al.*, "Multiplier architectures: Challenges and opportunities with plasmonic-based logic: (special session paper)," in *Proc. IEEE Des., Automat. Test Eur. Conf. Exhib.*, 2020, pp. 133–138.

[48] Y.-H. Kim, S.-H. Kwon, H.-S. Ee, Y. Hwang, Y.-S. No, and H.-G. Park, "Dependence of Q factor on surface roughness in a plasmonic cavity," *J. Opt. Soc. Korea*, vol. 20, no. 1, pp. 188–191, 2016.

[49] C. Min and G. Veronis, "Theoretical investigation of fabrication-related disorders on the properties of subwavelength metal-dielectric-metal plasmonic waveguides," *Opt. Exp.*, vol. 18, no. 20, pp. 20939–20948, 2010.

[50] C. Ciracì, F. Vidal-Codina, D. Yoo, J. Peraire, S.-H. Oh, and D. R. Smith, "Impact of surface roughness in nanogap plasmonic systems," *ACS Photon.*, vol. 7, no. 4, pp. 908–913, 2020.

[51] M. Urbieta *et al.*, "Atomic-scale lightning rod effect in plasmonic pico-cavities: A classical view to a quantum effect," *ACS Nano*, vol. 12, no. 1, pp. 585–595, 2018.

[52] S. Roberts, X. Ji, J. Cardenas, M. Corato-Zanarella, and M. Lipson, "Measurements and modeling of atomic-scale sidewall roughness and losses in integrated photonic devices," 2021, *arXiv:2105.11477*.

[53] W. Yu and R. Mittra, "A conformal finite difference time domain technique for modeling curved dielectric surfaces," *IEEE Microw. Wireless Compon. Lett.*, vol. 11, no. 1, pp. 25–27, Jan. 2001.

[54] E. D. Palik, *Handbook of Optical Constants of Solids*, vol. 3. New York, NY, USA: Academic Press, 1998.

[55] D. M. Caughey and R. Thomas, "Carrier mobilities in silicon empirically related to doping and field," *Proc. IEEE*, vol. 55, no. 12, pp. 2192–2193, 1967.

[56] C. Canali, G. Majni, R. Minder, and G. Ottaviani, "Electron and hole drift velocity measurements in silicon and their empirical relation to electric field and temperature," *IEEE Trans. Electron Devices*, vol. 22, no. 11, pp. 1045–1047, Nov. 1975.

[57] J. Fossum and D. Lee, "A physical model for the dependence of carrier lifetime on doping density in nondegenerate silicon," *Solid-State Electron.*, vol. 25, no. 8, pp. 741–747, 1982.

[58] G. Hurkx, D. Klaassen, and M. Knuvers, "A new recombination model for device simulation including tunneling," *IEEE Trans. Electron Devices*, vol. 39, no. 2, pp. 331–338, Feb. 1992.

[59] Z. Han, A. Elezzabi, and V. Van, "Experimental realization of subwavelength plasmonic slot waveguides on a silicon platform," *Opt. Lett.*, vol. 35, no. 4, pp. 502–504, 2010.